RESEARCH ARTICLE | NOVEMBER 16 2023

# Design and numerical assessment of an additively manufactured Schwarz diamond triply periodic minimal surface fluid-fluid heat exchanger

**Special Collection:** Proceedings of the International Congress of Applications of Lasers & Electro-Optics (ICALEO 2023)

Tim Röver ; Maxim Kuehne ; Floyd Bischop ; Leighton Clague ; Bastian Bossen ; Claus Emmelmann



*J. Laser Appl.* 35, 042071 (2023)
https://doi.org/10.2351/7.0001184

Journal of Laser Applications ARTICLE pubs.aip.org/lia/jla

# Design and numerical assessment of an additively manufactured Schwarz diamond triply periodic minimal surface fluid-fluid heat exchanger

Cite as: J. Laser Appl. 35, 042071 (2023); doi: 10.2351/7.0001184
Submitted: 17 July 2023 · Accepted: 13 October 2023 ·
Published Online: 16 November 2023



Tim Röver,[1] Maxim Kuehne,[1] Floyd Bischop,[2] Leighton Clague,[3] Bastian Bossen,[1] and Claus Emmelmann[1]

## AFFILIATIONS

[1]Institute of Laser and Systems Technology, Hamburg University of Technology, Harburger Schloßstraße 28, Hamburg 21079, Germany
[2]Institute of Product Development and Mechanical Engineering Design, Hamburg University of Technology, Denickestraße 17, Hamburg 21073, Germany
[3]Xerion Berlin Laboratories® GmbH, Gross-Berliner Damm 84 A, Berlin 12487, Germany

**Note:** Paper published as part of the special topic on Proceedings of the International Congress of Applications of Lasers & Electro-Optics 2023.



## ABSTRACT

In aerospace, thermal applications demand compact, lightweight, and efficient heat exchangers. Additive manufacturing processes offer the potential to create highly complex structures that are not achievable through traditional manufacturing methods. This work presents the development of an additively manufactured fluid-fluid heat exchanger that shows the potential to enhance the performance, reduce weight, and increase compactness compared to a conventional plate heat exchanger. A numerical model of the conventional plate heat exchanger was created, and fluid dynamics simulations with heat transfer were performed. Validation of the simulations was done by experiments. Then, a novel heat exchanger was designed using a bottom-up approach and investigated at different levels of complexity using computational fluid dynamics. The internal structure of the final heat exchanger consists of a repeating triply periodic Schwarz diamond minimum surface elongated in the direction of flow. The heat exchanger was manufactured with laser powder bed fusion process using AlSi10Mg. It had a 108% higher compactness and 54% lower weight compared to the plate heat exchanger. Numerical analysis yielded the pressure loss in pascal was reduced by 50%–59% while heat transfer in watts was improved by 3%–5%. Future researches should experimentally investigate the thermal and fluid mechanical characteristics of the novel additively manufactured heat exchanger and increase compactness and heat transfer further by analyzing the minimum partition wall thickness and the impact of wall roughness and deposit formation.

Key words: design for additive manufacturing (DfAM), heat exchanger, PBF-LB/M, AlSi10Mg, product development, laser additive manufacturing (LAM), computational fluid dynamics (CFD), triply periodic minimal surfaces (TPMS)



## I. INTRODUCTION

The aerospace industry is constantly seeking to improve the performance of components by aiming for weight reduction, efficiency increase, and compactness. In this context, additive manufacturing (AM) has emerged as a promising technology to achieve these goals. In particular, laser powder bed fusion of metals (PBF–LB/M) has become the most widely used metal processing AM technique. A major advantage of the process compared to conventional manufacturing processes is the possibility to produce highly complex structures, while producing high-quality parts which are fully dense and show similar or even higher tensile strength than conventional castings.[1]

AM also offers great potential in the field of thermal applications due to the custom material options and the possibility to manufacture complex internal structures. For instance, requirement-specific heat

exchangers (HEs) can be developed for heat transfer between fuel and engine oil in aerospace applications.[2] HE are thermal systems that transfer energy in the form of heat between at least two mediums. In fluid-fluid HE, the fluids are usually separated by a partition wall[3] and pass through the HE in opposite directions to maximize heat transfer.[4] Previous work indicates the potential of AM for the HE development. Using PBF-LB/M, Confux Technology was able to develop a HE that triples heat transfer compared to conventional HE, reduced pressure drop by two-thirds, and reduced weight by 22%.[5]

In the development of HE, the main goal is to maximize performance, namely, reduce the pressure losses over the HE, maximize the heat transfer between fluids, and achieve a low mass of the component. One possibility is to integrate internal cellular designs that are modeled based on natural structures.[6,7] These consist of a network of repeating interconnected unit cells.[8] They are of interest for lightweight applications due to their high specific stiffness at low density[9] and for improving heat transfer.[10] Nonstochastic periodic cellular structures are, for example, honeycombs (two-dimensional periodicity)[11] or triply periodic minimal surfaces (TPMS) (three-dimensional periodicity).[12] The latter can be described using implicit functions. Figure 1 shows a Schwarz diamond TPMS as well as its implicit description.

The literature shows that TPMS structures offer advantages for fluid-fluid heat exchangers. In TPMS, the volume is already divided into two partial volumes by design and a high surface-to-volume ratio is obtained.[13,14] Previous work shows that the use of TPMS structures can increase heat transfer between 15% and 100% compared to conventional HE.[13–16] The goal of this work was to develop a novel fluid–fluid HE. For this purpose, the advantages of AM were used to integrate TPMS structures into the HE. Due to its ability to create complex internal structures, AM is the only manufacturing process that is feasible for the production of TPMS structures. The aim was to increase compactness, reduce weight, and increase performance compared to a conventional plate heat exchanger (PHE). Increased performance is characterized by higher heat transfer with lower pressure loss. To achieve this, a conventional PHE was analyzed experimentally as well as by numerical fluid mechanics simulations. Subsequently, an additively manufactured HE (AMHE) was developed and evaluated based on the results of the PHE analysis.

## II. METHODOLOGY

The methodology used in this paper is shown in Fig. 2. This paper follows a methodological approach divided into two main parts: the development of a numerical replica of a conventional plate heat exchanger (PHE) and the development of an additively manufactured heat exchanger (AMHE).

In the first part of the paper, the focus is put on the development of a numerical simulation model of the PHE. As basis for the PHE, a model of the company WilTec is considered in this work.[17] The process was divided into problem analysis, model development, and validation of the developed model. Based on the results of the analysis, a detailed model of the PHE was developed. First, the geometry of the PHE was analyzed since no information on the geometric dimensions is available from the manufacturer. For this purpose, the PHE was cut open by electrical discharge machining (EDM) and measured. Subsequently, a CAD model of the HE was generated, which was used for the CFD and heat transfer simulation. The simulation was carried out with the *Simcenter STAR-CMM+*$^{TM}$ software (in the following referred to as *STAR-CCM+*$^{TM}$) from Siemens with version 16.02.009. The postprocessing of the calculations was done using *STAR-CCM+*$^{TM}$ and *Matlab*®. Finally, to ensure the accuracy and robustness of the developed simulation model, it was then validated against experimental data. This validation step ensures that the model correctly represents the thermal and fluid mechanical performance characteristics of the real PHE. Based on the results of the PHE analysis, the performance requirements for the development of the AMHE were defined.

The second part of the work focused on the development of the AMHE. For this, a bottom-up approach was used. This approach is based on the building block approach (BBA) and describes a methodology whereby the target product is investigated step by step on different levels of complexity. At each level, knowledge is accumulated, ensuring a high-quality end product.[18] The complexity levels were determined based on the requirements of the AMHE. The process starts at the lowest complexity level with the investigation of the TPMS structures, for which extensive literature research already existed. Based on the literature review, the most suitable TPMS structure was selected. At the further levels of complexity, model development was then carried out on the component, substructure, and product levels. At the component level,

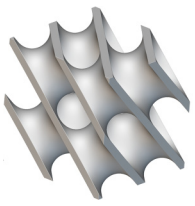

$$\begin{aligned}&\sin(x)\sin(y)\sin(z)\\&+\sin(x)\cos(y)\cos(z)\\&+\cos(x)\sin(y)\cos(z)\\&+\cos(x)\cos(y)\sin(z)\end{aligned} = 0 \quad (1)$$

**FIG. 1.** Schwarz diamond TPMS and implicit description of the cell.

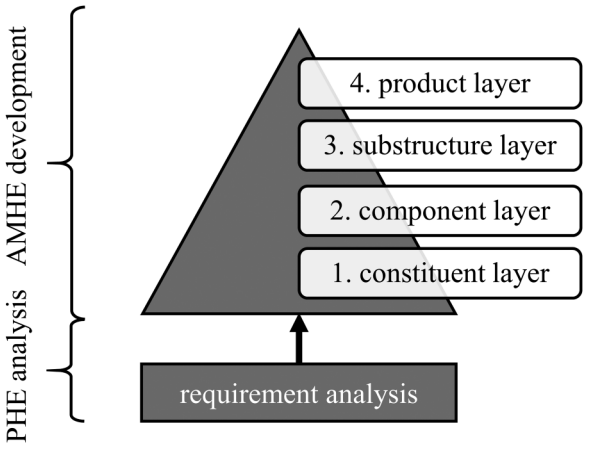


**FIG. 2.** Bottom-up methodology used for the development of the AMHE.

the influence of the size and stretching of the unit cell on the fluid mechanics and thermal properties was investigated and the minimum wall thickness needed between the fluids was determined. Based on the findings, a simplified model was created at the substructure level, which was used to investigate the influence of the connecting ports and manifolds. In the last development step, the design of the final AMHE was elaborated at the product level based on the results of the previous levels. The development of the AMHE with TPMS structures was done by implicit modeling using the nTopology® software (version 3.37.3).[19] Finally, the designed AMHE model was additively manufactured using the PBF-LB/M system MPrint+ from One Click Metal.[20]

## III. RESULTS

In the following, the results of the work are presented. Initially, the results of the PHE analysis are introduced and subsequently the results of the development of the AMHE are given.

### A. PHE analysis

As described in Sec. II, the first step was to analyze the PHE for the creation of a CAD model. Therefore, a detailed model of the individual plates is required. The individual plates of the PHE have a length of 154 mm, a width of 66 mm, and a thickness of 0.26 mm. They have an angle-wave embossing and are brazed together at the crests of the waves. The embossing has a depth of 2 mm with a wavelength of 7.75 mm. The brazing provides better support for the plates and an enlarged surface area for heat transfer. One of the two identical available PHE was cut open by EDM and the generated CAD model is shown in Fig. 3.[17]

#### 1. Simulation model

To set up the numerical simulation of the PHE and solve the discretized Navier–Stokes equations, a finite element model of the PHE was created. Therefore, the CAD model was imported to *STAR-CCM+*™ as a STEP file and the geometry was prepared by deriving partial volumes using *STAR-CCM+*™ operators. The simulation region ultimately consists of two partial volumes for the two fluids of the primary and secondary sides, as well as the solid volume (housing and plates of the PHE) separating the fluids.

Subsequently, meshing was used to convert the geometry into a discretized model for finite volume calculation. Meshing was performed in three steps. First, it was ensured that closed, so-called watertight volumes are present. Next, surface meshing was performed, in which the surfaces of the watertight volumes were meshed with triangular surfaces. Finally, volume meshing was performed, in which the volume of the computational domain was meshed with polyhedral elements. This element type is best suited for circulating flows.[21] To resolve the boundary layer near the surfaces of the fluid regions, prismatic cells were used. This allows a $y^+$ value below 1 to be achieved, which is required for the low Reynolds number turbulence model used.[22] Between the fluid regions and the solid region, conformal interfaces were used to account for heat transfer. The result of the meshing is shown in Fig. 4 using the central PHE cross section.

Next, the physical continuum is described by defining suitable physical models (e.g., solver, material model, and turbulence model). To numerically analyze the PHE, both the fluid flow and the heat transfer between the solid body and the fluids were considered. For this purpose, a conjugate heat transfer simulation was set up. The physical models used for the fluid and solid regions were selected according to the Siemens procedure for setting up conjugate heat transfer simulations.[21,23] The contact between the liquid and solid regions was simulated as a smooth wall due to the low surface roughness of the plates. A three-dimensional model was set up for the investigation of the PHE. Segregated models were selected for the fluid and solid energy conservation equations to account for heat exchange. A steady model was chosen. The turbulence model was based on the Realizable k-ε-two-layer model with the two-layer all $y^+$ wall treatment, which automatically selects the appropriate turbulence model depending on the $y^+$ value.

Furthermore, the initial and boundary conditions for the calculation area were defined. For the initialization of the temperature field, the temperature at the inlet of the cold fluid flow was used. Moreover, the computational domain must be constrained by appropriate descriptions at the boundaries.[24] The settings used for the features of the simulation software (in italics) are briefly explained below. The exchange of information between the fluid



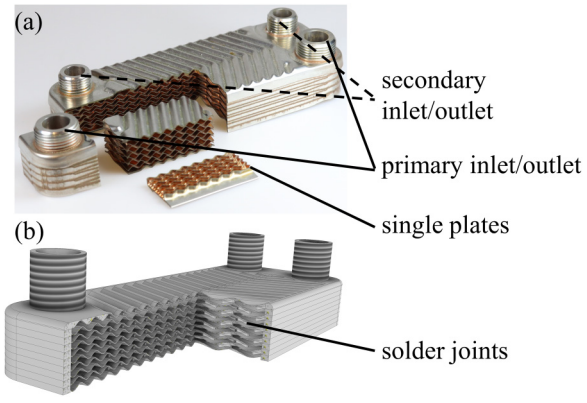


**FIG. 3.** (a) PHE cut open by EDM and (b) generated CAD model of the PHE.

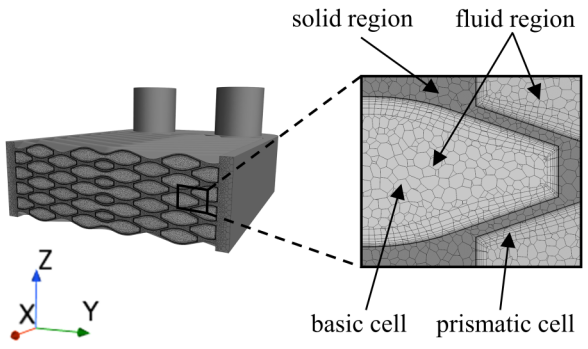


**FIG. 4.** Cross-sectional view of meshed PHE.

and solid regions was achieved, as explained earlier, through a conjugate interface that ensures the satisfaction of the continuity conditions. A Dirichlet boundary condition was used at the boundaries of the fluid region because the flow velocity at the wall is zero. The outer wall of the PHE was specified as an adiabatic wall. To model the flow of the domain, mass flow inlets were defined at the inlets of the primary and secondary sides. This was then used to directly regulate the mass flow for the fluid regions. The outlets were defined as pressure outlets with a pressure of 0 Pa and a defined velocity gradient. To monitor the pressure loss and temperature, *surface reports* were used that evaluate the average of the pressure and temperature across the surface at the inlets and outlets. The pressure loss was then calculated by subtracting the values of associated inlets and outlet. The physical models and boundary conditions used for the numerical simulation are summarized in Table I and are partly based on Ref. 21.

## 2. Validation of the simulation model

The numerical calculation was performed with 1000 iterations. At the end, the simulation converged to steady state. First, the mesh quality was investigated. Due to the low Reynolds number turbulence model used, a fine mesh ($y^+ < 1$) was required near the wall. Across the surface of the fluid regions, an averaged $y^+$-value of 0.341 was determined. Therefore, the used turbulent models are valid. Moreover, a mesh convergence study was performed, varying the base cell size and the number of prismatic cells. Then, the influence on the pressure drop and heat transfer was investigated. Both parameters showed a minor influence on the result variables with maximum differences of 1.5%.

**TABLE I:** Physical models and boundary conditions used in the numerical heat exchanger simulation

| | | |
|---|---|---|
| | Fluid continuum | Solid continuum |
| *Material phyisics* | Liquid | Solid |
| | Three Dimensional | |
| | Constant Density | |
| | Gradients | |
| *Heat transfer physics* | Segregated Fluid Temperature | Segregated Solid Energy |
| | Solution Interpolation | |
| *Solver setting* | Steady | |
| | Cell Quality Remediation | |
| *CFD physics* | Realisable k-ε Two-Layer | — |
| | Reynolds-Averaged Wavier-Stokes | — |
| | Segregated Flow | — |
| | Turbulent | — |
| | Two-Layer All $y^+$ Wall Treatment | — |

Validation of the simulation was carried out on the basis of a setup test bench shown in Fig. 5 by means of the piping and instrumentation diagram. Two independent water circuits were used, with flow rate controllable by ball valves and temperature regulated by an adjustable 600 W immersion heater. Both circuits were connected to the PHE in counterflow direction. Thermocouples, differential pressure sensors, and flow sensors were placed upstream and downstream of the PHE to determine the heat transfer and pressure loss for different volume flows.

Since the pressure loss is quadratically related to the flow velocity,[25] the experiments were performed for different volume flow rates and because the heat transfer is related to the Reynolds number, also for various Reynolds numbers. The pressure loss was determined by averaging the measurements over an interval of 60 s per operating point at volume flows between 3 and 20 l/min. Heat transfer measurement was done after a steady state was achieved. The temperatures in the water reservoirs are maintained within a constant range using an immersion heater. In line with the used type of measurement setup, a temperature range of 35–37 °C was set for the inlet of the primary side, while 10–12 °C was used for the inlet of the secondary side. The heat transfer rates were determined based on Reynolds number operating points, which were converted to volumetric flow rates using a MATLAB® script. The heat transfer was determined at Reynolds numbers 3000, 4750, and 6500. The experimental procedure involves setting the temperatures, calculating the flow rates, adjusting the flow rates using valves, and measuring temperature and flow rate once the system reaches steady state.

To validate the computation of the pressure loss, the influence of the experimental setup on the measured values was determined first. Furthermore, it had to be distinguished between the cold side of the PHE consisting of four fluid channels and the warm side of the PHE consisting of five fluid channels. For investigation of the

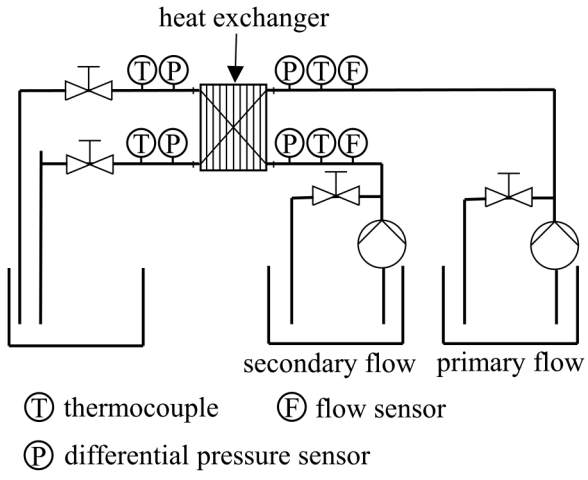


**FIG. 5.** Piping and instrumentation diagram of the experimental setup.

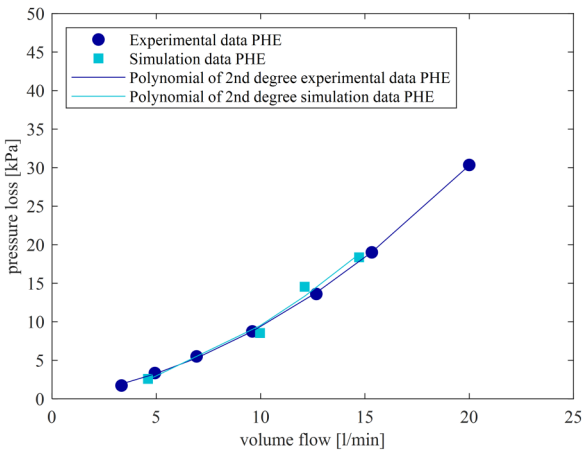


**FIG. 6.** Pressure loss for the experimental and simulation data for different flow rates on the primary side of the PHE.

pressure loss of the PHE, the warm side with five fluid channels was considered in this work. The diagram in Fig. 6 shows the experimentally and numerically determined pressure losses for various volume flows of the PHE as well as the second degree approximation polynomials. The curves show a strong fit between the measured data and the simulation results with a maximum deviation of 5.5%. Possible causes for these differences can be geometric deviations in the CAD model, measurement inaccuracies of the sensors or the selected turbulence models in the simulation.

The validation of the heat transfer calculation was done by measuring the temperature and volume flows at three operating points. The heat transfer of the primary and secondary sides are calculated based on Newton's law of cooling[26] using the average

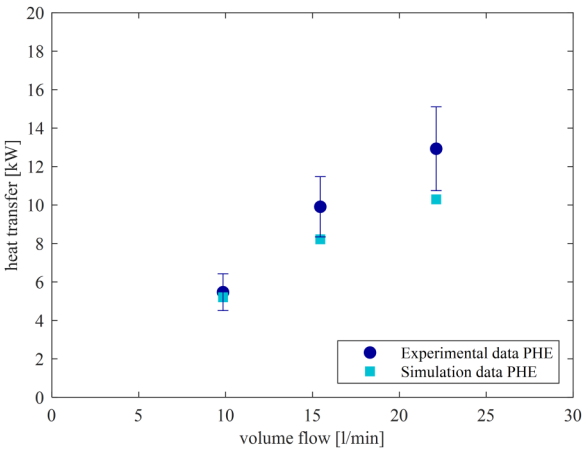


**FIG. 7.** Heat transfer for the experimental and simulation data for different flow rates on the primary side of the PHE.

temperature difference across the transfer surface. For the comparison, the results of the primary side are considered in the following. The results of the experimentally and numerically determined heat transfer are shown in Fig. 7. It can be seen that the deviation is smallest at a flow rate of 10 l/min with 5%. However, the deviation increases for larger flow rates. At a flow rate of 22 l/min, the experimentally determined heat transfer is 25.5% larger than the numerically calculated heat transfer. Potential causes for these differences are the geometric deviations of the CAD model, the modeling of the material properties or the turbulence model used. Especially the brazed joints are difficult to model and are assumed to be part of the plate in the simulation to minimize the computational effort. As a result, the material properties of the PHE plates are also assigned to them, which may affect the heat transfer.[27] Regarding the turbulence model, the study of Gullapalli and Sunden[28] shows that the turbulence models tend to underestimate the heat transfer by 20%–30%. This will be considered in the remainder of this paper.

Overall, the results of the PHE analysis show that the simulation is able to model the pressure drop to high accuracy and heat transfer up to an error of 25.5%, which was deemed acceptable. For the development of the AMHE, the performance requirements are derived from the PHE analysis. The determined characteristics of the PHE are summarized in Table II.

## B. AMHE development

The goal for the development and design of the AMHE was to achieve a reduced weight, an increased heat transfer and a reduced pressure drop compared to the analyzed PHE. As previously explained, the development of the AMHE followed the bottom-up approach, through the step-by-step consideration of different levels of complexity.

### 1. Constituent level

The first step was to determine a suitable TPMS structure for the AMHE at the constituent level. Various TPMS structures have been studied in the literature with respect to heat transfer between fluids,[15,29,30] and the diamond and gyroid TPMS have been found to be advantageous.[13,16] For rather large Reynolds numbers up to 20 000, both structures show similar results in terms of heat transfer and pressure drop.[13] However, for smaller Reynolds numbers up to 300, the diamond TPMS was preferred because of its larger transfer surface area.[15] Furthermore, a study by Kim and Yoo[16] showed that the diamond TPMS has higher heat transfer than the gyroid TPMS for the same pressure loss. Moreover, the diamond TPMS show the greatest surface-to-volume ratio of the considered cells.[16] Based on these results, the diamond TPMS was selected for further investigation in this work.

For the computer-aided development of the AMHE, an initial model with diamond TPMS structures was first built using *nTopology*. A *rectangular volume lattice* was defined as construction space ($40 \times 20 \times 20\ \text{mm}^3$), which was filled with the diamond TPMS. The size of the unit cells was defined by a period length in x-, y-, and z-directions, allowing the cell to be stretched targeted in the respective directions. Boolean operations were used to generate two separate volumes for the fluids and the partition thickness was

**TABLE II.** Physical, thermal, and fluid flow properties of the PHE on the primary side.

| | | | | | |
|---|---|---|---|---|---|
| Physical properties | Weight | | 560 | | g |
| | Heat transfer surface | | 1200 | | $cm^2$ |
| | Compactness | | 274 | | $m^2/m^3$ |
| Thermal and fluid flow properties | Operating point | 1 | 2 | 3 | |
| | Flow rate | 10 | 15 | 22 | l/min |
| | Heat transfer | 5.47 | 9.91 | 12.93 | kW |
| | Pressure loss | 8.75 | 19.04 | 40.37 | kPa |

set. Finally, the geometry was converted to a surface mesh and exported as a CAD/STL file. It is noted that analysis of the wall thicknesses of the STL files as exported from nTopology yielded a certain variation of the wall thicknesses in the final STL geometries. Therefore, mean wall thicknesses of $0.25 \pm 0.05$ and $0.16 \pm 0.02$ mm were considered within this study and referred to as 0.25 and 0.16 mm throughout this work, respectively.

### 2. Component level

At component level, the minimum, additively manufacturable wall thickness between the fluids was first determined experimentally. The partition wall represents a thermal resistance. Therefore, the goal was to achieve the smallest possible wall thickness of a tight wall in order to maximize the heat transfer. The main limitation is the PBF-LB/M method. If the wall thickness is too small, the partition walls can become porous and result in mixing of the fluids.

Wall thicknesses of 0.16 and 0.25 mm were tested at different pressure levels. Specimens with a volume of $40 \times 40 \times 20$ $mm^3$, filled with diamond TPMS (period length $20 \times 10 \times 10$ $mm^3$ in the corresponding spatial directions), were used for this purpose. For an optical leak test, one fluid side was sealed and filled with water via an inlet. Figure 8 shows the additively manufactured TPMS structure with a wall thickness of 0.25 mm for leak testing. The experiment showed that a wall thickness of 0.16 mm leads to visible cracks between the TPMS structure and cover plate that results in leaking. For the 0.25 mm specimen, no defects were visible and the structure was tight for all tested pressures. Therefore, a partition wall thickness of 0.25 mm was used.

A preliminary numerical study on the TPMS core structure was done to investigate the influence of the size and elongation of the unit cell in the flow direction on the thermal and fluid mechanical properties. As with the PHE, the contact surface between the liquid and solid regions was simulated as a smooth surface to ensure comparability of the simulation results with the PHE simulations. The rough surface resulting from AM was neglected. Three simplified AMHE models were considered, where the period length of the unit cell is identical in the three spatial directions and set to 5, 10, and 15 mm. The simulation results for the pressure loss and the heat transfer are shown in Fig. 9. According to this, a reduction of the unit cell size from 10 to 5 mm leads to a 225% higher pressure loss and a 114% increased heat transfer due to the 66% larger transfer area.

The simplified AMHE models and their simulation results are shown in Fig. 10. The simulation shows that a 5 mm cell results in higher flow velocities. Consequently, higher velocity gradients perpendicular to the wall occur and higher wall shear stresses develop, leading to frictional pressure losses which is in line with the literature.[31] Figure 10(b) shows the significantly increased wall shear stresses for the 5 mm unit cell compared to the other models. The higher pressure drop can be attributed to said frictional pressure losses. Likewise, the increased heat transfer can be accounted for by the higher wall shear stresses which is in line with literature.[13]

Furthermore, the stretching of the unit cell was investigated. The transfer area and turbulent mixing are increased in TPMS structures compared to straight ducts, but related to higher pressure loss due to the undulations.[13] In order to find a balance between

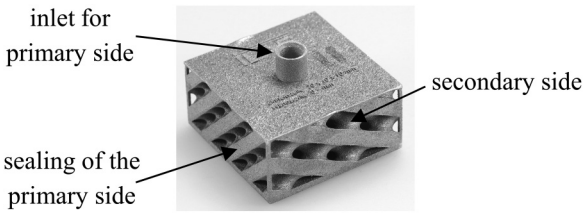


**FIG. 8.** Specimen for leak testing.

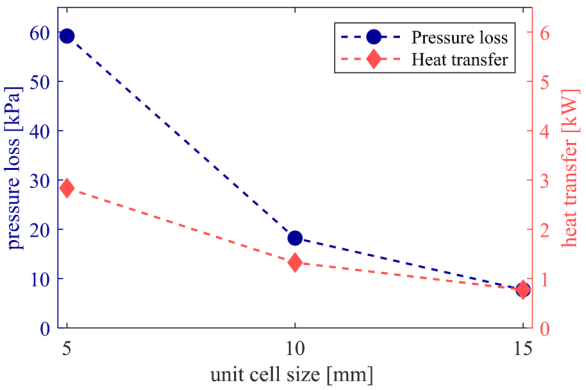


**FIG. 9.** Influence of unit cell size on the pressure loss and heat transfer on the component level.

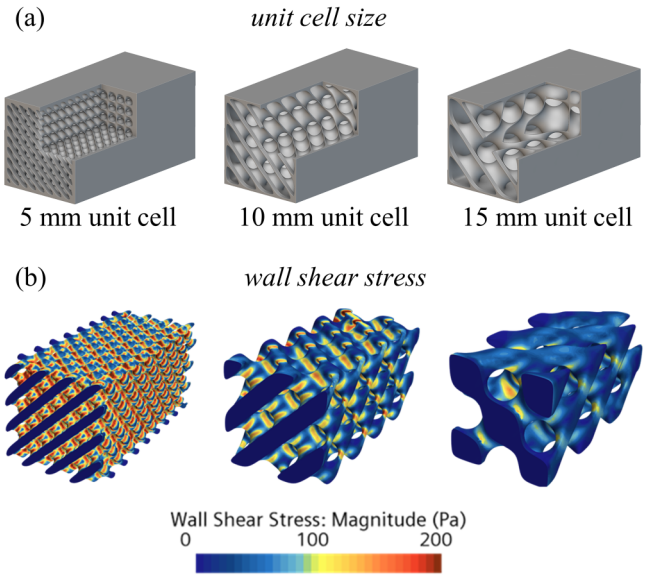


**FIG. 10.** (a) Models for the unit cell size investigation and (b) simulation results of the wall shear stresses.

transmission area, turbulent mixing and pressure loss, the unit cell was stretched in the main flow direction ($x$ axis). The period length of the TPMS unit cell can be adjusted independently in spatial directions. The investigation was performed by gradually increasing the period length in the x-direction by 10 mm, starting from a simplified HE with a $10 \times 10 \times 10\ \text{mm}^3$ unit cell.

Figure 11 shows the computation results for the pressure losses and heat transfer as a function of the period length in the x-direction. The plot shows that a period length of 30 mm results in a significant reduction in pressure loss of approximately 95% and in heat transfer of approximately 52%. As described, the results in this case can also be explained by the wall shear stresses, which

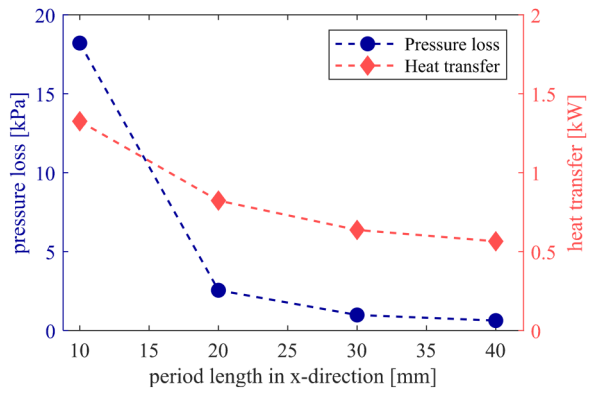


**FIG. 11.** Influence of the period length in the x-direction on the pressure loss and heat transfer on the component level.

are significantly lower for a unit cell size of 30 mm and, accordingly, the pressure loss is also reduced. Consequently, a period length of at least 20 mm is aimed at for the stretching of the unit cell.

### 3. Substructure level

Next, a simplified model was constructed at the substructure level. The design was developed with the requirement that the pressure drop would be below and heat exchange above that of the PHE to obtain a design with higher performance characteristics compared to the PHE (see Table II). The substructure level development did not consider the connection nozzles and manifolds. Due to the beneficial volume-to-external surface ratio, a cylinder with a height of 100 mm and a diameter of 50 mm was used as the design space (see Fig. 12). To prevent cracks, as in the case of the leak tests, rounded fillets were included into the design at the transition between the TPMS structure and the outer wall of the cylinder. This design was expected to be less prone to cracking. Based on the results at component level, a stretched unit cell with a wall thickness of 0.25 mm was used. The period length was set to 10 mm in the x-direction and 5 mm in the y- and z-directions. The numerical analysis of the cylinder showed that the model does neither meet the defined thermal performance requirements using a $20 \times 10 \times 10\ \text{mm}^3$ nor using a $10 \times 5 \times 5\ \text{mm}^3$ unit cell compared to the PHE. Therefore, a smaller unit cell ($8 \times 4 \times 4\ \text{mm}^3$) was used. This adaptation increases the transfer surface area and the heat transfer coefficient so that the requirements with respect to the PHE were met. Consequently, the smaller unit cell was used for further investigation at the product level.

### 4. Product level

For the product-level investigation of the connecting ports and manifold geometry, the arrangement of the connection nozzles and the distribution of the flow in the channels of the TPMS structure were examined. Both a uniform distribution of flow is important,[32] as is the pressure loss across the manifold, which should be lower than across the TPMS structure. For a valid comparison between PHE and AMHE, the same inlet flow cross section ($201\ \text{mm}^2$) of the manifolds was used. The influence of the inlet and outlet orientations of the connecting nozzles was investigated using three variants. As a basis for the variants, a cylinder with rounded ends was used as the build space for the TPMS structure. The connection nozzles were arranged in a counterflow design and connected to

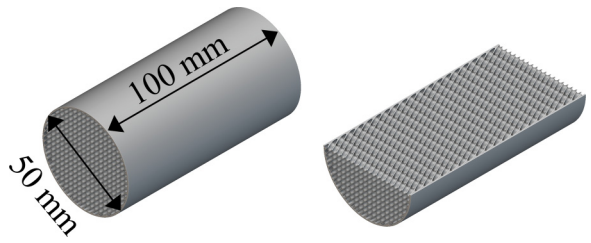


**FIG. 12.** Cylindric simulation model on the substructure level.

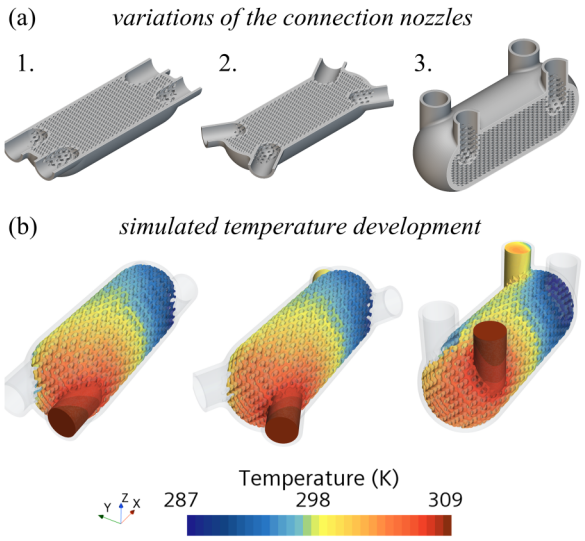


**FIG. 13.** (a) Variations of the connection nozzle arrangement and (b) simulation result of the temperature field.

each other via the internal TPMS structure. The inner diameter of the connecting branches is 16 mm. The three variants are shown in Fig. 13(a) and include a linear arrangement of the connecting nozzles (1), a rotation of 26.5 degrees from the center plane outward (2), and an upward arrangement similar to the PHE (3).

The numerical results show that variant 1 has a 10% higher pressure loss and a 4% greater heat transfer compared to variant 3. The lower pressure drop and heat transfer in variant 3 are caused by the design of the manifold and the position of the connection nozzles. Due to the smaller spacing of the connection nozzles, the flow length to the outlet is shorter. At the same time, the arrangement of the connection nozzles in variant 3 leads to an uneven distribution of the flow in the TPMS heat exchanger core in which the velocities and volume flows are lowest in the bottom section of the AMHE. Comparison of the temperature fields [see Fig. 13(b)] also show that temperature distribution between the connecting nozzles in variant 3 is uneven, which emphasizes the importance of uniform flow distribution for improved heat transfer.[32] Variant 2,

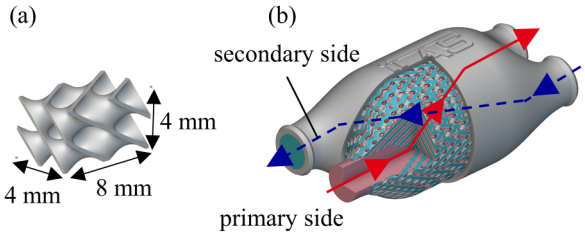


**FIG. 14.** Final solutions for (a) the Schwarz diamond TMPS cell and (b) the AMHE.

**FIG. 15.** Additively manufactured AMHE.

in which the connecting nozzles are aligned based on a main flow direction in the TPMS structure, has a 4% lower pressure loss compared to variant 3 and a 1% higher one compared to variant 1. All three variants meet the pressure loss and heat transfer requirements, with variant 1 being preferred due to the highest heat transfer. In addition, variant 1 enables additive manufacturing without support structures if the connection nozzles of one side are positioned on the build platform and the manifold is adjusted accordingly to limit the overhang angle to 45°.

Combing the insights from all previously presented results, the final design of the AMHE was developed. At the substructure level, a diamond TPMS unit cell with a period length of 8 mm in the x-direction and 4 mm in the y- and z-directions was selected [see Fig. 14(a)]. Stretching in the flow direction reduces the undulation of the channels, which reduces the pressure loss. The unit cell was chosen to be 4 mm in the y- and z–directions to increase the transmission area and compactness of the AMHE compared to the PHE. Based on the results on the orientation of the connection nozzles, a counterflow design with a crossflow manifold was selected. The inner diameter of the connecting nozzles was set to 16 mm which is in line with the connecting nozzles of the PHE. Consequently, the core flow cross section of the connecting nozzles is 201 $mm^2$, while the flow cross-section of the inner, conical manifold into the TPMS structure is increased to 560 $mm^2$, resulting in a reduced pressure loss. In addition, a converging conelike shape was introduced for the final design based on Ref. 32 to achieve a small pressure drop across the manifold. For the AMHE, a wall thickness of 0.25 mm was used for the partitions and 2 mm for the outer walls to ensure mechanical integrity. Figure 14(b) shows the designed model in a three-quarter section view.

## 5. Additive manufacturing of the AMHE

The manufacturing preparation was done with *Autodesk Netfabb Ultimate Slicer* software (version 2023.1). Additive manufacturing was carried out using the PBF-LB/M system MPrint+ from One Click Metal. Aluminum alloy AlSi10Mg (Ref. 33) was used. The fabrication was performed with a laser power of 170 W, a scanspeed of 1200 mm/s, a hatch distance of 0.1 mm, a 20 $\mu$m layer thickness, and a focus diameter of 70 $\mu$m. The finished AMHE is

**TABLE III.** Geometric characteristics of the PHE and AMHE.

| | PHE | AMHE | Change (%) |
|---|---|---|---|
| Weight (g) | 560 | 254 | −54 |
| Heat transfer surface ($cm^2$) | 1200 | 1466 | 22 |
| Compactness ($m^2/m^3$) | 274 | 570 | 108 |
| Volume ($cm^3$) | 438 | 257 | −41 |

shown in Fig. 15. Experimental characterization of the novel additively manufactured heat exchanger will be done by the authors in future works. The printed part will potentially differ from the simulation, e.g., in terms of surface roughness, fabricated inclination angles, and interaction of solid and medium. This can affect the accuracy of the numerical results in this study.

## IV. COMPARISON OF PHE AND AMHE

In the following, the AMHE is evaluated against the defined requirements based on the PHE based on the simulation results.

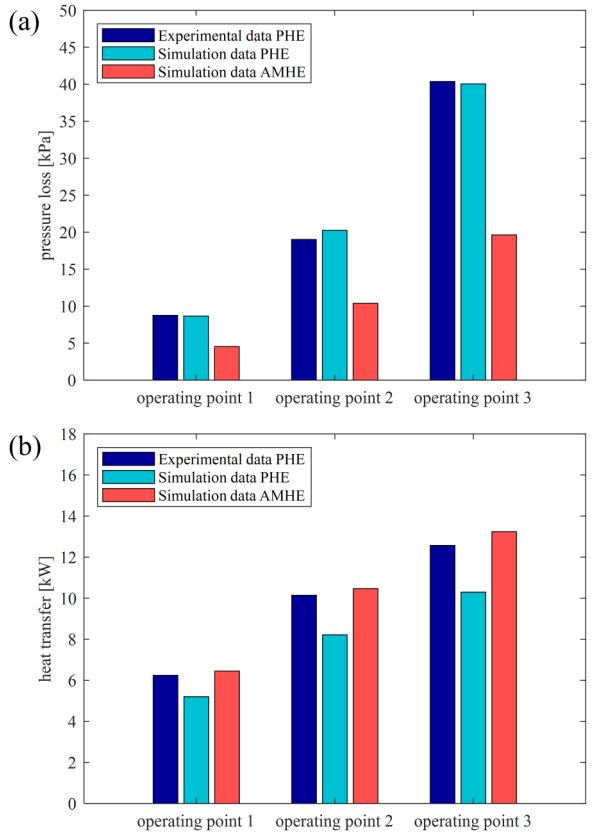


**FIG. 16.** (a) Pressure loss of PHE (experimental) and AMHE (simulation). (b) Heat transfer of PHE (experimental and simulation) and AMHE (simulation) for the primary side.

Weights of the PHE and the AMHE were measured using a precision scale.

First, the geometrical characteristics of the AMHE are evaluated. Table III compares the main characteristics of the HEs. Compared to the PHE, the manufactured AMHE shows a significant reduction of 54% in weight and 41% in volume, while increasing the compactness by 108% and heat transfer area by 22%. Thus, the AMHE has been significantly improved in all geometrical parameters compared to the PHE. The improvements can mainly be attributed to the possibilities of the PBF-LB/M process to produce complex geometries and to the lower density of the material used for the AMHE.

Furthermore, the performance of the AMHE is analyzed. For the comparison, the values of the primary side are considered. Figure 16 shows the experimental and numerical data of the PHE and the numerical data of the AMHE for the pressure loss (a) and heat transfer (b) for the considered operating points. Figure 16(a) shows that the pressure loss of the AMHE is 50%–59% lower compared to the PHE for all three operating points. Figure 16(b) shows that the heat transfer of the AMHE is 3%–5% higher for all operating points when comparing to the experimental data of the PHE and about 26%–30% higher when compared to the simulation data of the PHE. Consequently, the requirements for the AMHE in terms of pressure loss and heat transfer are met by the results of the numerical simulation. When evaluating the results, it should be noted that the comparison of the simulation with the experimental data of the PHE showed that numerical analysis underestimated the heat transfer by about 20%–30%. This deviation is considerable, which is why experimental validation must be carried out for a definitive evaluation of the AMHE's performance characteristics. Nevertheless, the potential of the novel AMHE can be concluded from the simulation results as it can be assumed that the actual heat transfer of the AMHE is even higher than the simulation results.



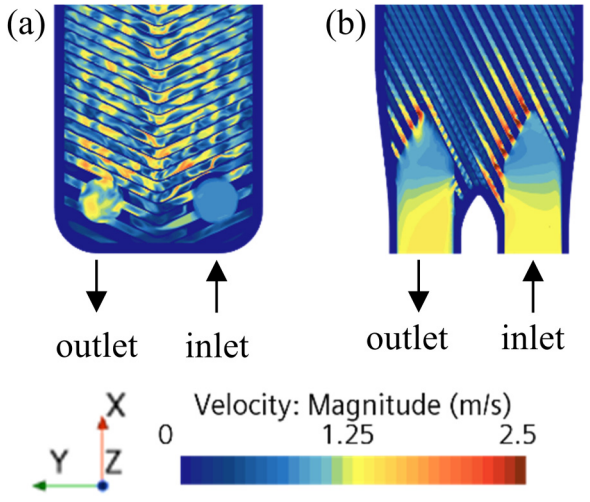


**FIG. 17.** Velocity field for the primary inlets of the (a) PHE and (b) AMHE.

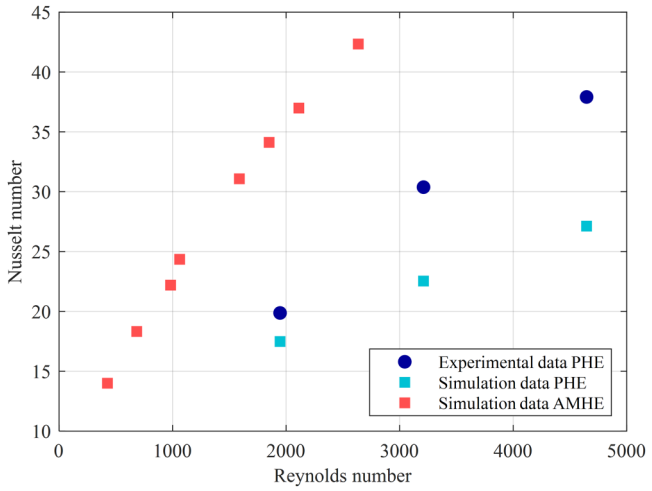


**FIG. 18.** Reynolds–Nusselt diagram.

The AMHE shows a lower pressure drop compared to the PHE (60% lower at operating point 2). This is due to lower friction, deflection and turbulence losses. The numerical simulation shows a lower flow velocity in the channels of the AMHE due to its larger cross section compared to the PHE. Accordingly, the Reynolds number of the AMHE is 59% lower than that of the PHE for the same flow rate. As a result, the wall shear stresses and frictional pressure losses are reduced for the AMHE. The increased pressure drop of the PHE can be attributed to deflection and turbulence losses. These are caused by the brazed joints in the PHE, which lead to recirculation regions downstream of the joints. In the AMHE, these effects are probably less pronounced due to the stretching of the TPMS structure.[34] In addition, the comparison of flow velocities (see Fig. 17) shows that for the AMHE these are significantly increased at the transition to the TPMS structure, resulting in a pressure gradient that does not occur in case of the PHE. This can be attributed to the TPMS structure. Due to its three-dimensional shape, half of the inlets into the channels are unfavorable in terms of fluid mechanics.

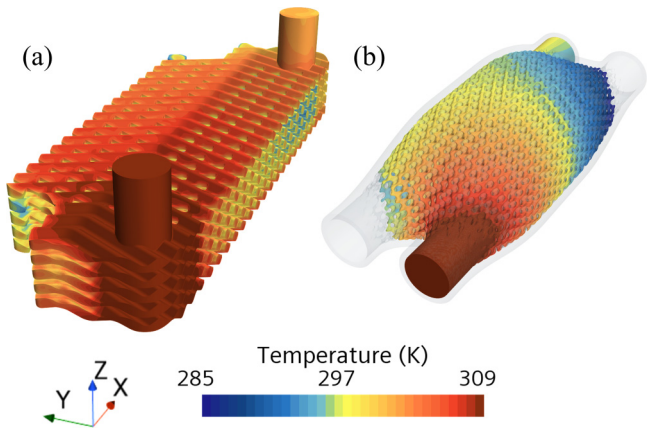


**FIG. 19.** Temperature distribution of the PHE (a) and AMHE (b) on the primary side.

To estimate the heat transfer properties of the AMHE and the PHE, the measured volume flow rates were converted into Reynolds numbers and the heat transfer coefficients were given in the form of the average Nusselt number. The hydraulic diameter of the HEs was used as the characteristic length for calculating the two performance indicators. Due to its larger cross section, the AMHE has lower Reynolds numbers at same flow rates. The results are shown in Fig. 18. The Nusselt numbers increase with Reynolds number for both HE and are about 30%–40% higher for the AMHE. The higher Nusselt numbers of the AMHE indicate a higher heat transfer in the boundary layer.

The numerical simulation results show that the temperature distribution on the surface of the AMHE is more homogeneous than for the PHE (see Fig. 19). In particular, the temperatures at the cover plates are increased. This is explained by the TPMS structure, which increases the transfer area by 22% and enhances heat transfer due to undulations and turbulence production.[13]

In terms of performance, the pump power required for the transferable heat transfer is considered. This indicates that the AMHE can be assumed to be more efficient, especially at low volume flows. As the volume flow rate increases, the difference decreases rapidly. According to Li *et al.*,[13] this is the result of combined effects from the transfer area and turbulence production. At higher volumetric flow rates, turbulence production dominates heat transfer, and at low rates, the larger transfer area is critical.

## V. CONCLUSION AND OUTLOOK

In this work, a novel fluid-fluid HE was developed using AM. The goal was to increase compactness, reduce weight, and improve performance compared to a conventional PHE. A model of the PHE was created and validated to provide comparative data for the AMHE. CAD models, conjugate heat transfer simulations, and experimental studies were used to determine the PHE model error. Discrepancies up to 25.5% between simulation and measured data were found and attributed to geometric discrepancies, accuracy of numerical turbulence models, and measurement inaccuracies. The AMHE was developed using a bottom-up approach and elaborated based on a Schwarz diamond TPMS structure. Additive manufacturing of the AMHE was done in the PBF-LB/M process using AlSi10Mg as a material of choice. Numerical simulation results were used to estimate the performance AMHE against the PHE. Simulation results show a significant 50%–59% reduction in pressure loss, 3%–5% improvement in heat transfer, and 108% increase in compactness and 54% weight reduction compared to the PHE.

It is noted that the simulated values provide only an estimate of the potential to this point and require experimental validation to allow definitive statements about the performance of the AMHE to be drawn. Nevertheless, the results of the work show the great potential of AM in the field of fluid-fluid HE and demonstrate a corresponding methodology for developing novel HE. The capability to easily generate complex structures and the use of material-

specific properties regarding lightweight design and heat transfer, which can be optimally exploited through the use of simulations and AM, prove to be the main advantages of the approach in this work.

Future works should focus on the experimental characterization of the novel additively manufactured heat exchanger and its comparison to the PHE as well to the numerical results for validation. Furthermore, improving the measurement accuracy of the test rig, optimizing the manifold geometry and further studies on the partition wall thickness are identified as potential research approaches to further improve the performance systematically. In addition, it is recommended to investigate the influence of wall roughness and deposit formation within the TPMS structure on the performance of the AMHE.

## ACKNOWLEDGMENTS

The authors would like to thank Jürgen Wittkamp (iLAS) and Maximilian Keller (iLAS) for additive manufacturing of the AMHE. Moreover, the authors acknowledge that the master's theses of Jonathan Scott Evenson (iLAS, 2017) and Kevin Janzen (iLAS, 2019) were helpful for conducting this study. Furthermore, the authors thank the Forschungswerkstatt Maschinenbau of TUHH for carrying out the EDM on the conventional HE and the additively manufactured HE. Additionally, the authors thank the Fraunhofer IAPT for permission to use its experimental test set up for characterization of fluid-fluid HE.

## AUTHOR DECLARATIONS

### Conflict of Interest

The authors have no conflicts to disclose.

### Author Contributions

T.R., M.K., and F.B. contributed equally to this paper.

**Tim Röver:** Conceptualization (equal); Investigation (supporting); Methodology (equal); Supervision (lead); Validation (supporting); Writing – original draft (supporting); Writing – review & editing (equal). **Maxim Kuehne:** Validation (supporting); Writing - original draft (lead); Writing - review & editing (equal). **Floyd Bischop:** Conceptualization (supporting); Investigation (lead); Methodology (equal); Validation (lead); Writing – original draft (supporting); Writing – review & editing (equal). **Leighton Clague:** Conceptualization (lead); Investigation (supporting); Methodology (equal); Supervision (lead); Validation (supporting). **Bastian Bossen:** Supervision (equal); Validation (supporting); Writing – review & editing (supporting). **Claus Emmelmann:** Conceptualization (supporting); Supervision (supporting); Writing – review & editing (equal).

## REFERENCES

[1]R. Lachmayer, R. B. Lippert, and T. Fahlbusch, *3D-Druck beleuchtet: Additive Manufacturing auf dem Weg in die Anwendung* (Springer Vieweg, Berlin, 2016).
[2]G. Bräunling, *Flugzeugtriebwerke: Grundlagen, Aero-Thermodynamik, ideale und reale Kreisprozesse, thermische Turbomaschinen, Komponenten, Emissionen und Systeme*, 3rd ed. (VDI-Buch) (Springer, Berlin, 2009).
[3]W. Polifke and J. Kopitz, *Wärmeübertragung: Grundlagen, analytische und numerische Methoden*, 2nd ed. (Ing—Maschinenbau) (Pearson Studium, München, 2009), see https://ebookcentral.proquest.com/lib/kxp/detail.action?docID=5574931.
[4]P. Böckh and T. Wetzel, *Wärmeübertragung: Grundlagen und Praxis*, 5th ed. (Springer Berlin Heidelberg, Berlin, 2013).
[5]EOS GmbH, "Case Study: Our First Patented Design," see https://www.confluxtechnology.com/article/case-study-conflux-s-first-patented-heat-exchanger (accessed 22 June 2023).
[6]R. Attarzadeh, M. Rovira, and C. Duwig, "Design analysis of the 'schwartz D' based heat exchanger: A numerical study," Int. J. Heat Mass Transfer **177**, 121415 (2021).
[7]H. Peng, F. Gao, and W. Hu, *Design, Modeling and Characterization of Triply Periodic Minimal Surface Heat Exchangers with Additive Manufacturing* (University of Texas at Austin, 2019).
[8]I. Gibson, D. W. Rosen, B. Stucker, and M. Khorasani, *Additive Manufacturing Technologies: 3D Printing, Rapid Prototyping, and Direct Digital Manufacturing* (Springer, Cham, 2021).
[9]T. A. Schaedler and W. B. Carter, "Architected cellular materials," Annu. Rev. Mater. Res. **46**, 187–210 (2016).
[10]T. J. Lu, H. A. Stone, and M. F. Ashby, "Heat transfer in open-cell metal foams," Acta Mater. **46**, 3619–3635 (1998).
[11]T. Bitzer, *Honeycomb Technology: Materials, Design, Manufacturing, Applications and Testing*, 1st ed. (Chapman & Hall, London, 1997).
[12]E. Lord and A. Mackay, "Periodic minimal surfaces of cubic symmetry," Curr. Sci. **85**, 346–362 (2003), see https://www.semanticscholar.org/paper/Periodic-minimal-surfaces-of-cubic-symmetry-Lord-Mackay/7f6d2dfb25542d34399807fed21c4277aba299a9.
[13]W. Li, G. Yu, and Z. Yu, "Bioinspired heat exchangers based on triply periodic minimal surfaces for supercritical $CO_2$ cycles," Appl. Therm. Eng. **179**, 115686 (2020).
[14]M. Alteneiji, M. I. H. Ali, K. A. Khan, and R. K. A. Al-Rub, "Heat transfer effectiveness characteristics maps for additively manufactured TPMS compact heat exchangers," Energy Storage Saving. **1**, 153–161 (2022).
[15]T. Femmer, A. J. C. Kuehne, and M. Wessling, "Estimation of the structure dependent performance of 3-D rapid prototyped membranes," Chem. Eng. J. **273**, 438–445 (2015).
[16]J. Kim and D.-J. Yoo, "3D printed compact heat exchangers with mathematically defined core structures," J. Comput. Des. Eng. **7**, 527–550 (2020).
[17]WilTec Wildanger Technik GmbH, "Bedinungsanleitung Plattenwärmetauscher," see https://service.wiltec.de/manuals/50/50671/DE/50671-oc-de.pdf (accessed 24 June 2023).
[18]B. F. Backman, *Composite Structures, Design, Safety and Innovation*, 1st ed. (Elsevier, Amsterdam, 2005).
[19]nTopology, "Next-Gen Engineering Design Software: nTop (formerly nTopology)," see https://www.ntop.com/ (accessed 24 June 2023).
[20]One Click Metal, "BOLDSERIES—Technische Daten—One Click Metal MPrint +," see https://oneclickmetal.com/de/boldseries-technische-daten/ (accessed 24 June 2023).
[21]Steven Dowding, "Best Practices for Modeling Heat Transfer in Simcenter STAR-CCM+," see https://community.sw.siemens.com/sfc/servlet.shepherd/document/download/0694O00000BGQn1QAH?operationContext=S1 (accessed 30 April 2023).
[22]R. Schwarze, *CFD-Modellierung: Grundlagen und Anwendungen bei Strömungsprozessen* (SpringerLink Bücher) (Springer, Berlin, 2013).
[23]A. G. Siemens, "Simcenter STAR-CCM+ User guide," see https://training.plm.automation.siemens.com/mytraining/libraries.cfm?mem=TG22000&library=Simcenter%20STAR%2DCCM%2B (accessed 24 June 2023).
[24]S. Lecheler, *Numerische Strömungsberechnung: Schneller Einstieg durch anschauliche Beispiele mit ANSYS 15.0*, 3rd ed. (Lehrbuch) (Springer Vieweg, Wiesbaden, 2014).
[25]W. Wagner, *Wärmeaustauscher: Grundlagen, Aufbau und Funktion thermischer Apparate*, 5th ed. (Kamprath-Reihe) (Vogel Business Media, Würzburg, 2015).

[26]J. H. Lienhard, *A Heat Transfer Textbook* (Dover Publications, New York, 2020).
[27]S. Jin and P. Hrnjak, "Effect of end plates on heat transfer of plate heat exchanger," Int. J. Heat Mass Transfer **108**, 740–748 (2017).
[28]V. S. Gullapalli and B. Sundén, "CFD simulation of heat transfer and pressure drop in compact brazed plate heat exchangers," Heat Transfer Eng. **35**, 358–366 (2014).
[29]J. Feng, J. Fu, X. Yao, and Y. He, "Triply periodic minimal surface (TPMS) porous structures: From multi-scale design, precise additive manufacturing to multidisciplinary applications," Int. J. Extreme Manuf. **4**, 022001 (2022).
[30]S. S. Rathore, B. Mehta, P. Kumar, and M. Asfer, "Flow characterization in triply periodic minimal surface (TPMS)-based porous geometries: Part 1—Hydrodynamics," Transp. Porous Media. **146**, 669–701 (2023).
[31]H. Herwig and A. Moschallski, *Wärmeübertragung: Physikalische Grundlagen und ausführliche Anleitung zum Lösen von Aufgaben*, 4th ed. (Springer eBooks Computer Science and Engineering) (Springer Vieweg, Wiesbaden, 2019).
[32]B. Zohuri, *Compact Heat Exchangers: Selection, Application, Design and Evaluation* (Springer, Cham, 2017).
[33]Fehrmann Alloys GmbH & Co. KG, "Materialdatenblatt Aluminiumpulver AlSi10Mg," see https://www.fehrmann-materials.com/sites/fehrmann-hamburg.de/files/Datasheet/AlSi10Mg-techDatasheet.pdf (accessed 24 June 2023).
[34]P. Stephan, S. Kabelac, M. Kind, D. Mewes, K. Schaber, and T. Wetzel, *VDI-Wärmeatlas: Mit 1046 Abbildungen und 483 Tabellen*, 12th ed. (VDI Springer Reference) (Springer Vieweg, Berlin, 2019).